Temperature-dependent droplet impact dynamics of a water droplet on hydrophobic and superhydrophobic surfaces: an experimental and predictive machine learning–based study

S. Keshavarzi[1*], J. Sourati[2], G. Momen[1], R. Jafari[1]

[1]Department of Applied Sciences, University of Québec in Chicoutimi, Chicoutimi, Québec, Canada

[2] University of Chicago, Illinois, IL, USA

Corresponding author: Samaneh Keshavarzi,

Email address: samaneh.keshavarzi1@uqac.ca

Abstract

Heightening the water repellency of surfaces can serve anti-icing purposes by removing water drops before they freeze and adhere to a surface. Here we study the impact dynamics of water droplets on silicone rubber surfaces—ranging from hydrophobic to superhydrophobic—at −20, −10, and 25 °C. We evaluate the influence of static contact angle, contact angle hysteresis, surface roughness, temperature, impacting velocity, and droplet diameter on droplet behavior (e.g., deposition, bouncing, splash). Minor effect of temperature on droplet dynamics on microstructured surfaces for a wide range of Weber and Reynolds numbers is observed. Experimental observations show that full bouncing only occurs on superhydrophobic surfaces with a CA > 160° and a CAH < 2° at temperatures above 0 °C for *We* <110 and *Re* <5000. Increasing the impact velocity of the droplet on rough surfaces heightens the probability of splashing. This experimental data is then coupled with machine-learning techniques (logistic regression, decision tree, and random forest) to comprehensively investigate droplet impact behavior on hydrophobic and superhydrophobic surfaces at various temperatures. We predict the behavior probability of impacting droplets on surfaces as a function of Weber number, Reynolds number and surface features (static contact angle, contact angle hysteresis, temperature, and surface roughness). Our experimental results and machine learning–based predictions are highly consistent, demonstrating that machine learning can effectively predict droplet motion on hydrophobic and superhydrophobic silicone rubber surfaces at different temperatures.

Keywords: superhydrophobic, surface features, temperature, droplet impact, freezing, machine learning

1. Introduction

Ice formation on structures poses a major hazard for exposed infrastructure and equipment and can lead to serious incidents, including aircraft crashes, the collapse of transmission lines, and damage to industrial facilities [1–4]. Ice removal techniques from solid surfaces can be classified into active de-icing and passive anti-icing methods. The latter means offers numerous advantages over active de-icing [5–7]. Passive anti-icing includes icephobic surfaces, which prevent ice formation on the surface without requiring external energy. These icephobic surfaces usually operate by exhibiting an improved water repellency (droplet mobility) to remove water droplets before their freezing, hinder ice nucleation on the surface, reduce the ice adhesion force, or a combination of these properties [8–11].

Improving our knowledge about ice nucleation, ice formation, and ice adhesion processes can help overcome issues related to surface icing and enhance the design of icephobic surfaces. Superhydrophobic surfaces can be very effective in preventing ice formation compared with hydrophilic or hydrophobic surfaces because of their ability to repel impacting droplets before ice nucleation [12,13]. Nonetheless, some studies have reported the opposite effect of superhydrophobicity on ice mitigation [14,15].

Much focus has been placed on ice accretion and the related impact and freezing processes of water droplets on cold surfaces [16–19]. The impinging of a droplet on a surface leads to a conversion from inertial energy to surface energy, droplet spreading, and droplet deformation. The wetting properties of surfaces and the extent of energy dissipation when a droplet lands on a surface produce various impact droplet patterns [20]. For superhydrophobic surfaces, the pure conversion of kinetic energy into surface energy is expected because the air pockets trapped at the interface minimize the dissipation of the kinetic energy of the droplet. Thus, bouncing is possible because of the sufficient energy stored in deformation during droplet impact. However, high-energy dissipation for other surfaces, such as hydrophilic surfaces, reduces the kinetic energy available for bouncing [21,22].

Different phenomena arise during droplet impaction onto a solid surface, such as deposition, receding, splashing, and bouncing [23]. The outcome of an impacting droplet is determined by multiple factors, including droplet properties (e.g., viscosity, density, surface tension), operational parameters (e.g., velocity), and surface characteristics (e.g., wettability) that are altered by surface roughness or texturing [24–26]. Dimensionless parameters are used to account for these factors affecting droplet impact dynamics. These critical parameters include the Reynolds number, $Re = \rho u_0 d_0/\mu$, the Weber number, $We = \rho {u_0}^2 d_0/\sigma$, the capillary number, $Ca = \mu u_0/\sigma$, and the Ohnesorge number, $Oh = \mu/\sqrt{\rho\sigma d_0}$, where u_0 is the impact velocity, d_0 is the initial droplet diameter, and ρ, μ, and σ are the liquid density, viscosity, and surface tension, respectively [27]. Surface wettability is commonly stated in terms of the contact angle (CA) of a water droplet and contact angle hysteresis (CAH), which is the difference between the advancing and receding CAs. The latter is often used as a measure of droplet mobility across a surface.

A critical characteristic affecting liquid droplets on cold solid substrates is surface temperature. Under icing conditions, water droplet properties, wetting properties, and frost formation depend greatly on surface temperature and cause the impacted water droplet to move less rapidly across the cold surface [28]. The effect of substrate roughness and temperature on droplet impact dynamics on cooled superhydrophobic surfaces has been discussed by Maitra et al. [29]. They found that the critical Weber number for the droplet impalement was independent of the substrate temperature. However, Alizadeh et al. [29] reported a strong temperature dependency for the impact dynamics of water droplets on hydrophilic to superhydrophobic surfaces at a Weber number of 138. Lower substrate temperatures lead to less droplet retraction. Zheyan et al. [30] reported the detailed dynamic motions of a water droplet impacting an ice surface and concluded that the lowering of the ice surface temperature decreases the maximum spreading factor.

Much effort has been placed on investigating the impact behavior of water droplets on cold superhydrophobic surfaces; however, most of these studies have been confined to narrow parameter ranges. Mishchenko et al. [31] focused on the design of ice-free nanostructured surfaces and evaluated droplet behavior on supercooled nano- and microstructured surfaces able to repel impacting water before ice nucleation. They performed impact tests using 15 μL water droplets falling from 10 cm onto cold surfaces (−25 to −30 °C) and found that the rebounding process was suppressed on surfaces colder than −25 °C. Ding et al. [32] investigated the effect of superhydrophobic surface inclinations and the degree of supercooling on water droplet dynamics. In their study, a 14 μL water droplet was projected at 0.99 $m \cdot s^{-1}$ onto a superhydrophobic surface having a static CA of 160 ± 1°. They observed that the droplet successively underwent full rebound, partial rebound, and no rebound as surface temperatures decreased. Zheng et al. [33] demonstrated that supercooled droplets impacting inclined and dry superhydrophobic surfaces can bounce off without freezing because of a reduced surface contact time and contact area of the impinging water droplets on properly designed surfaces. Finally, Li et al. [34] investigated the influence of a supercooled water droplet on cold hydrophilic and superhydrophobic surfaces. They observed that solidification of a 1.6 mm diameter supercooled droplet impacting a cold superhydrophobic substrate at 3.4 $m \cdot s^{-1}$ reduced droplet bouncing.

Most research in this area has focused on the outcome of droplet regimes relying on a few select parameters. Critically, these studies lack an analysis incorporating all possible parameters, especially as the droplet impact process is a complex interaction of multiple variables, as discussed above. However, the development of machine learning–based methods that can consider all influential parameters affecting impacting droplet behavior can offer some design criteria for water-repellent superhydrophobic surfaces subjected to various temperatures. Machine learning can support engineering tasks to manage and extract insights from the resulting data [35,36]. Furthermore, these approaches can reduce the high costs and time required for carrying out multiple complex experiments.

Artificial intelligence and statistical-learning methods are increasingly used in various fields, such as computer science, material science, and aircraft icing research [37–39]. For example, Zhang et al. [40] used artificial neural networks and evolutionary computation to enhance our understanding of superhydrophobic surfaces by determining the relationship between water droplet volume, nanoparticle weight, the falling distance between the superhydrophobic surface and the water droplet, and multiple properties (droplet CA, sliding angle, and adhesive force). Li et al. [41] also applied machine learning to predict the severity of aircraft icing in relation to various conditions, including liquid water content, droplet diameter, and exposure time. Although it is possible to examine the effect of various parameters in conventional experimental investigations, machine-learning models improve our ability to find patterns within large data sets.

There is currently no comprehensive study that has examined the influence of surface characteristics on the dynamic behavior of water droplets at different temperatures while incorporating machine learning approach. In our previous work [42], we investigated the drop dynamic behavior on hydrophobic and superhydrophobic surfaces at room temperature in line with finding some design criteria (in terms of surface CA, CAH, and roughness values) based on machine learning approach to improve the feasibility of achieving the bouncing of drops when they impact on hydrophobic and superhydrophobic surfaces. The goal of the presented research is to investigate temperature dependency of water droplet impact on hydrophobic and superhydrophobic surfaces and coupling the experimental results with machine learning-based methods for prediction of the drop dynamic behavior at different temperatures. It is worth mentioning that this new article complements the previous article by examining the temperature dependency of the droplet dynamic, using linear and nonlinear methods of machine learning to predict the droplet dynamic, providing different equations for prediction the droplet behavior and studying the relative importance of affecting parameters on water droplet impact.

In this paper, we study the temperature dependency of impact dynamics. We quantify the influence of drop properties, kinematic parameters, and surface characteristics on impacting droplet behavior (e.g., deposition, bouncing, and splashing) on silicone rubber surfaces (hydrophobic to superhydrophobic). A machine-learning technique is applied to evaluate the outcome regime of impact droplet behavior based on CA, CAH, temperature (T), and the root mean square surface roughness value (S_q), *We* and *Re* numbers. We demonstrate that machine learning can effectively predict droplet impact behavior. We formulate three different methods using a decision tree, random forest, and logistic regression to develop a data-driven approach for predicting droplet impact behavior by exploring the complex interactions between CA, CAH, S_q, T, and the *We* and *Re* numbers. Our experimentation and machine-learning approach is a novel means of investigating droplet behavior on hydrophobic to superhydrophobic surfaces at different temperatures. Moreover, we develop correlations through logistic regression for predicting the behavior probability of impacting droplets as a function of the analyzed parameters. We selected these three machine-learning methods for predicting impact droplet behavior, as they are state-of-the-art techniques having a strong predictive capability.

2. Material and Methods

2.1. Sample preparation

High-temperature vulcanized (HTV) silicone rubber was used as the process material. A chemical-etching method was used to produce microstructured aluminum templates (A6061) using a 4.8, 9.8, 14.8, 19.8 wt% hydrochloric acid solution and immersion of aluminum templates in this solution for 2 h. A micro-compression molding machine with two temperature-adjustable platens (Carver Inc. USA) was used to mold the rubber samples. The hydraulic press system can precisely control an applied force of 3 to 194 kN [24]. The rubber material is cast in three pieces of flat molds, each with a right rectangular prism cavity of 25 x 15 x 6 mm^3. After the template was placed in the cavity, the rubber material was placed over it. Next, the top of the mold was closed. The mold was set in the press machine to begin the process. In the press machine, the following mold parameters were set: a molding pressure of 35 MPa, a curing time of 4.7 minutes, and a mold temperature of 149 °C. After the process was complete, the mold was opened, and the silicone rubber with the size of 25 x 15 x 6 mm^3 was removed from the aluminum template (Fig. 1).

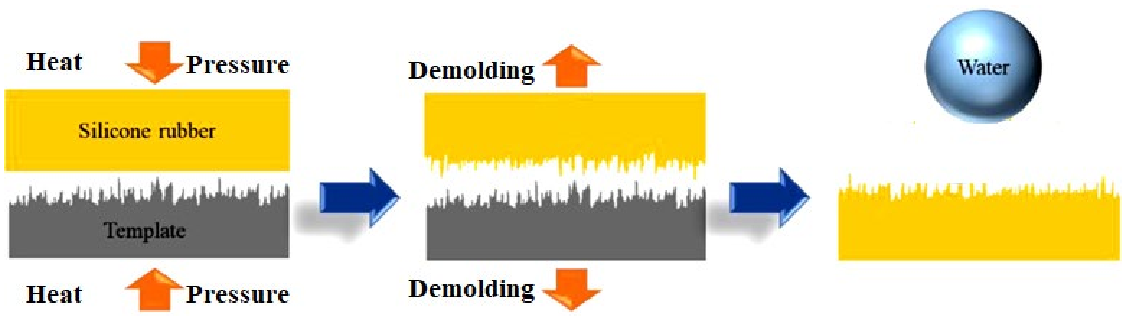

Fig. 1 Schematic of the fabrication of micro-nanostructured silicone rubber surfaces via a microcompression molding technique [21]

2.2. Surface Characterization

Using a Kruss™ DSA100 goniometer at 25 °C, we measured the water CA using a water droplet of 4µL deionized water based on the method of Young-Laplace. A CAH is equal to the difference between the advancing and receding contact angles when a droplet moves on the surface. All wettability measurements were taken at five different points on each sample to ensure accuracy and reproducibility. For each sample the average and standard deviation were reported. The surfaces were characterized using a confocal laser microscopy profiler (Profil3D, Filmetrics, USA) and a scanning electron microscope

(JSM-6480 LV, JEOL Japan). In Fig. 2, the surface structures of different samples are presented as SEM images and 3D profiles.

In the case of Sample1, which was replicated on a smooth aluminum template, it exhibited hydrophobic surface characteristics (due to its low surface energy), while the other samples exhibited superhydrophilicity (because they were replicated on aluminum templates with varying acid concentrations). Therefore, to fabricate superhydrophobic surfaces, we used a low-surface-energy material with intrinsic hydrophobicity, combined with a sufficient level of surface roughness. In the Sample 2, 3, 4, and 5 samples, S_q increased by 1.87, 3.77, 4.49, and 4.28 respectively compared to sample1. Table 1 shows CA, CAH, and S_q of these five microstructured surfaces.

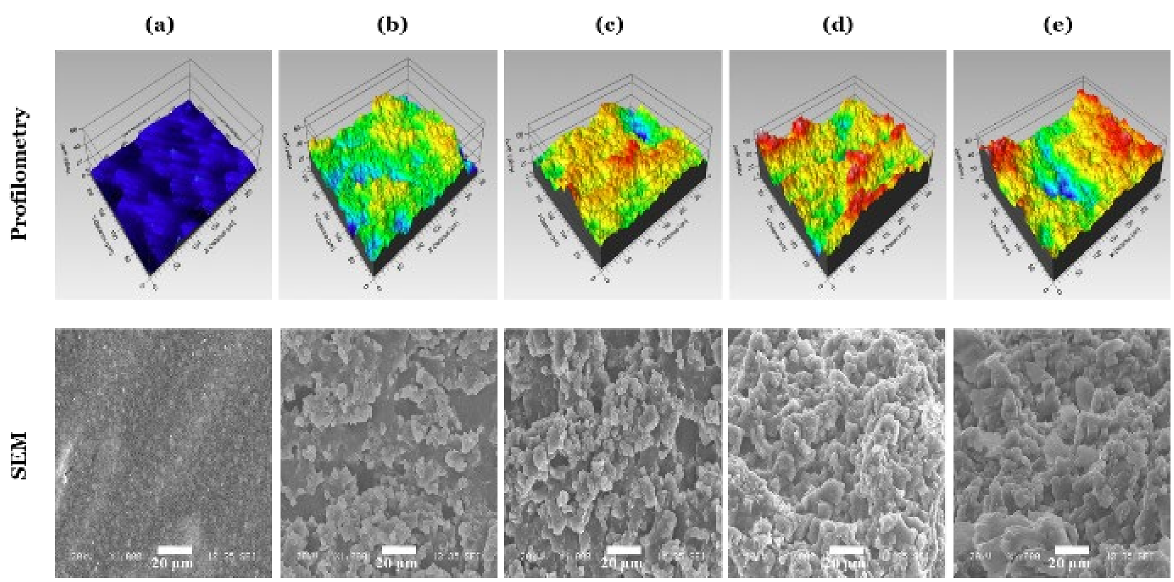

Fig. 2 The 3D surface profiles and SEM images of samples (a) 1, (b) 2, (c) 3, (d) 4, and (e) 5 [42].

Table 1 Surface characteristics of hydrophobic and superhydrophobic surfaces and kinematic parameters used in the experiments. For all samples, falling velocity (u_0) varied between 0.4 and 2.7 m/s, droplet size (d_o) was either 2.67 or 3.02 mm, and the surface temperatures (T) were −20, −10, and 25 °C

Sample No.	CA (°)	CAH (°)	S_q (µm)
1	116.0 ± 2	46.5 ± 2.4	1.76 ± 0.17
2	154.5 ± 1.4	28.0 ± 1.6	3.29 ± 0.4
3	165.3 ± 1.1	1.5 ± 0.2	6.64 ± 0.32
4	166.6 ± 0.9	0.6 ± 0.3	7.90 ± 0.24
5	162.8 ± 0.9	1.3 ± 0.8	7.54 ± 0.33

2.3. Experimental Setup

The experimental freezing setup included a thermally insulating and optically transparent chamber, high-speed camera, thermostatic bath, cold base, droplet injection system, test samples, data acquisition system, temperature sensor, humidity sensor, and a vibration-free table (Fig. 3). The double layer chamber that is thermally insulating and optically transparent will be used to control the temperature of humidity of experiment and affecting parameters on ice nucleation to be uniform during the experiment and increase the accuracy and reproducibility of the experiments. Its transparency would facilitate imaging of the freezing droplet. By having a small interior chamber (150 mm length ×150 mm width ×110 mm height) inside a large chamber (420 mm length ×420 mm width × 400 mm height), the droplet could be subjected to a uniform environment. During the cooling process, the relative humidity of the chamber can be controlled with a constant flow of dry nitrogen gas (N_2). We adjusted the temperature of the cold base using a thermostatic bath. The chamber's temperature and relative humidity were around 25 °C and 40% ± 3%, respectively. A high-speed camera and LED illuminator monitored the droplet impact process and visually recorded the droplet movement on the surfaces.

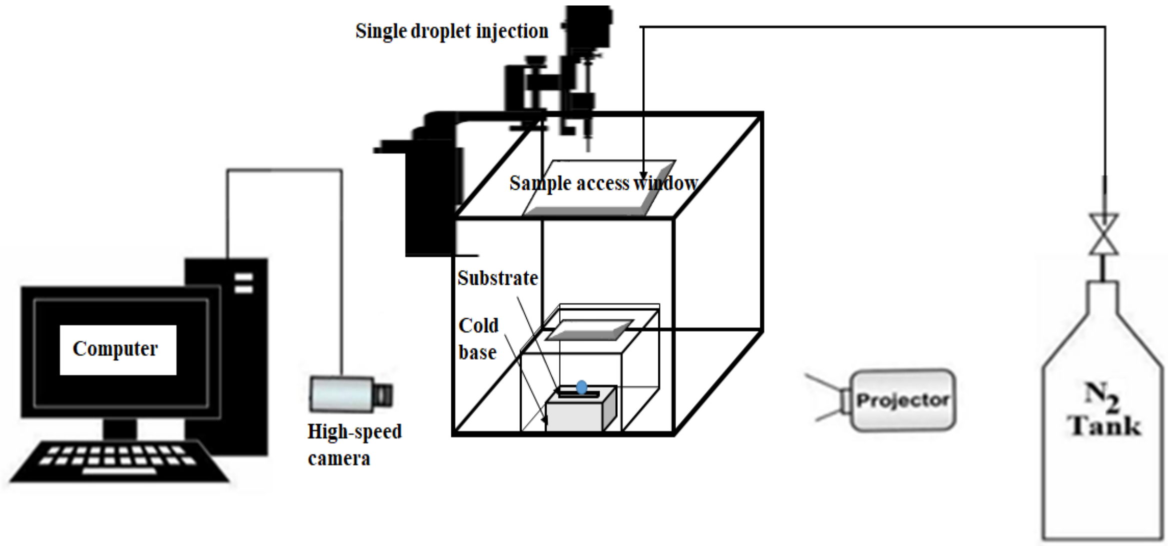

Fig. 3 Schematic of the experimental setup

We used two different syringe nozzles to vary drop diameters, all the spherical water droplets had a fixed volume of 10 µL (2.67 mm in diameter) and 20 µL (3.02 mm in diameter). We released 2.67 and 3.02 mm diameter droplets at room temperature from a droplet injection system at various heights, corresponding to initial droplet impact velocities ranging between 0.4 and 2.74 $m \cdot s^{-1}$. We placed a high-speed camera (MotionBLITZ, MIKROTRON, EoSens Cube 7, Germany) to record the droplet impact behavior at 3000 fps. Before each test, we adjusted the plate's temperature to either 25, −10, or −20 °C and placed the sample on the plate. We repeated each test (a specific combination of parameters) at least three times. We computed the impact velocity of the droplets from the elapsed distance and time recorded by the camera and the ImageJ software [42]. All experimental parameters, including the droplet properties, surface characteristics, surface temperature, and impact velocity, are summarized in Table 1.

2.4. Machine-Learning Methods

Among the various machine-learning methods, regression and classification are the most commonly used methods. To predict impacting droplet behavior on the silicone rubber surfaces, we applied three machine-learning models: logistic regression (LR), decision tree (DT), and random forest (RF). DT machine-learning models partition the feature space into several decision regions by successively dividing the space through simple decision rules, where each rule can be as simple as thresholding a single feature [43]. Each decision region is then assigned a single class label based on the class of its training samples. When the tree is fully constructed, the class of any given test sample is predicted by identifying the decision region into which the sample falls. These models are applicable to multiclass and nonlinear classification problems.

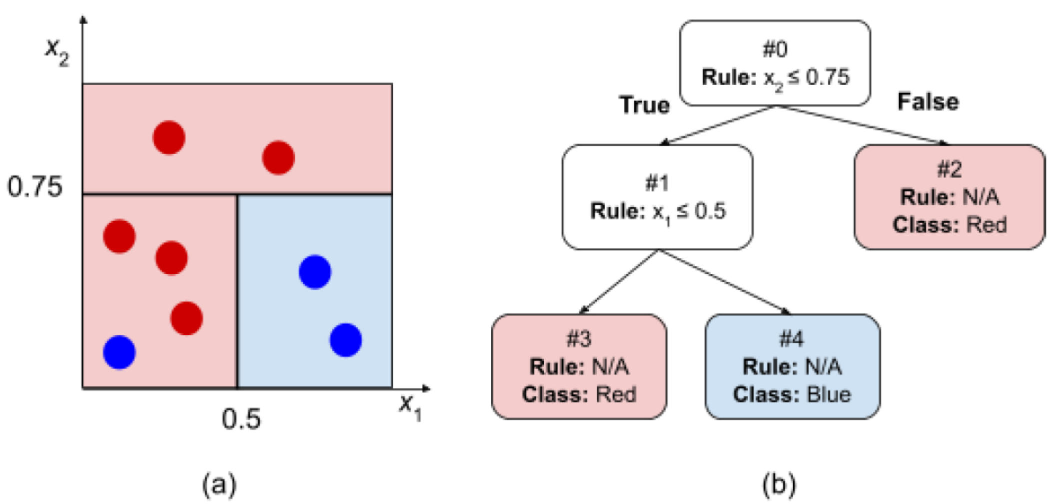

Fig. 4. An example illustrating DT classifier. (a) A 2D feature space corresponding to a data set with 2D feature vectors. The training samples are shown with red and blue circles with their color representing the class. The space is partitioned by a DT classifier trained over the training examples. (b) DT classifier that is trained over the training samples.

Fig. 4 shows an example of how a DT partitions 2-dimensional feature space of a 2D data with red (five labeled samples) and blue classes (three labeled samples). The left figure

(Fig. 4(a)) indicates the partitioning of the space, where the color of each region represents the class label assigned to it (red shadow for class red and blue shadow for class blue). The right figure (Fig.4(b)) shows the corresponding DT as a tree structure where each node contains a rule in the form of a feature thresholding. If the rule is satisfied for any test sample (True), we choose the left node in our next step, otherwise (False) we go to the right node. Starting from the root node (#0), we keep choosing nodes based on the nodes' rules until we get to a node without any children. Such nodes are usually called "leaves". Each leaf is associated with a partition in the feature space and is assigned a class label based on the class majority of the training samples belonging to that partition. In our example in Fig. 4, node #2 is a leaf that corresponds to the horizontal rectangle at the top of Fig. 4(a) which has two red training samples, hence is assigned the red class. Any test that falls in this partition (i.e., $x_2 \geq 0.75$) will be predicted as a "red" sample.

Training a decision tree starts from the root node corresponding to the entire feature space, where a feature and a cut-off threshold are selected so that the selected feature partitions the data into two groups having the highest possible sample homogeneity. Each partition forms a new node in the tree, where the same procedure is repeated to further divide the data set into two additional leaves. The divisions continue until either all the paths have reached the maximum number of divisions from the root, i.e., maximum depth (denoted by d_{max}), or all the leaves are assigned partitions with a sample homogeneity higher than a pre-specified threshold. Nodes at which splitting is stopped are referred to as leaves. When classifying the groups of data, the homogeneity of samples is inversely defined on the basis of the impurity of their class labels. Lower impurity implies higher homogeneity, and the smallest impurity is achieved when the class labels of all samples are identical. In our experiments, we used the Ginni index to measure class impurity, defined as:

$$Ginni = 1 - \sum_{i=1}^{c} P_i^2, \qquad \text{Eq. 1}$$

where P_i denotes the empirical distribution of the i^{th} class. We also ensured that all leaves contained at least one sample.

Training the DT can easily lead to an over-partitioning of the feature space, which, in turn, implies overfitting and instability. A common approach to alleviate this issue is to build an ensemble of trees via bootstrapping, a method commonly referred to as random forest (RF). This method consists of constructing multiple DTs, each separately trained with a distinct randomized data set that is obtained by sampling with replacement from the original data set [44]. Each tree in the forest will make an individual prediction of the class label of a test sample, and the final prediction will be reported through majority voting. In contrast to individual trees, RFs can assign a probability to their inferences, enabling an uncertainty analysis of the results. In our experiments, we trained 50 DTs to build our RF.

For an alternative approach, we also tried logistic regression (LR) in our experiments as a linear classifier that is widely used because of its simplicity [45]. This model is a single-layer neural network where the output undergoes a softmax function (a function in form of $e^{z_i} / \sum_{j=1}^{n} e^{z_j}$ for normalizing a set of real-valued scores $z_1, \ldots, z_n$) to generate a probability distribution, which is to be interpreted as the probability of belonging to different classes. Compactly representing this model, given the input vector $x = [x_1, \ldots, x_6]$ = [T, *Re*, *We*, CA, CAH, S_q], LR produces the output as the probability that x belongs to class i ($1 \leq i \leq 6$):

$$P(y = i \mid x) = e^{\beta_{i1}x_1+\dots+\beta_{id}x_d} / \sum_{j=1}^{6} e^{\beta_{j1}x_1+\dots+\beta_{jd}x_d}, \qquad \text{Eq. 2}$$

where $\beta_i = [\beta_{i0}, \beta_{i1}, .., \beta_{i6}]$ denotes the parameters corresponding to the i^{th} class. The exponents of these class probabilities are also known as the log-likelihood of the data sample x given the parameter values β_i, $1 \le i \le 6$. In the training step, parameters are tuned by maximizing (through the gradient ascent) the summation of the log-likelihood terms of the training data given their observed class labels plus a regularization penalty term that is usually in the form of the L1 [46] or L2 [47] norm of the parameter vectors. We used the latter in our experiments with a regularization coefficient of 1. Note that log-likelihoods are linear with respect to the data features; hence, logistic regression is known to have a lower class separability power than DT and RF, which experience greater nonlinearity.

2.4.1. Prediction Rules

2.4.1.1. Decision Tree

Class prediction in DT models includes following a set of simple decision rules over individual features. To keep our discussion concise, here we visualize only our shallowest DT model ($d_{max} = 4$) and demonstrate how class is inferred through its branches and leaves. The tree structure and trained parameters of this model are shown in Fig. 5, in which each tree node (*rectangle*) is labeled by its parameters and training data statistics. The first line of each node specifies the node ID. The second line shows the node's decision rule as an inequality for an individual feature. These inequalities divide the feature space into two halves producing one "child" node per partition. Moreover, a set of multiple inequalities collectively defines a partition (subregion) of the feature space. Each node in our tree is assigned a feature space partition that is determined by the set of its ancestors' inequalities. For instance, the root is assigned the whole feature space because it has no ancestors (hence, no partitioning), and the partition for Node #3 is defined by the inequalities {$S_q \leq 3.281$, $We \leq 87.925$}. The leaves do not have decision rules as they lack descendants. The third line in each node indicates the Ginni index value of the class labels for all the training samples falling inside the node's partition. Two more properties are present inside the leaves (i.e., nodes without descendants): "class sizes," explicitly listing the class distribution of the training samples inside the corresponding partitions, and "class," representing the predicted class inferred by the leaf. The inferred class is determined by the class having the largest number of training samples in the leaf's partition. Furthermore, class probabilities are obtained by estimating the empirical distribution from the class sizes.

Decision-tree predictions (class assignment) for any given test sample begin from the root node (#0), shown at the top of the tree, and move forward sequentially by choosing the next node based on the current node's decision rule. This sequential decision-making task ends once it reaches a leaf. Using Fig. 5, we can follow, as an example, the test sample with the feature values x = [T, Re, We, CA, CAH, S_q] = [−10, 3303.94, 52.22, 166.6, 0.6, 7.9]. Starting from the root node, the first decision rule we consider is $S_q \leq 3.281$. Given that our test's S_q is 7.9, the rule's inequality does not hold, and therefore, we choose Node #2 (the child node on the right in the figure) as our next node. The decision rule for Node #2 is $We \leq 87.925$, which does hold in the case of our test sample ($We = 52.22$). Therefore, we choose Node #3 (the left child of Node #2 in Fig. 5) as our third step. Repeating this procedure, we encounter the decision rule $T \leq 24.843$ in Node #3, which holds; thus, we move to Node #4, followed by decision rule $Re \leq 3526.178$, which also holds; hence we move to Node #5. At Node #5, our prediction procedure ends because there are no further descendants. The predicted class in this leaf is PB (Fig. 5). To measure the uncertainty of this prediction, we can compute the empirical class distributions by normalizing the class sizes such that they sum to one. From Fig. 5, the class sizes are [0, 55, 0, 297, 8, 0] (the total number of training samples in Node #5's partition is 55 + 297 + 8 = 360). Normalizing, this yields the empirical distribution [0, 55/360, 0, 297/360, 8/360, 0] = [0, 0.153, 0, 0.825, 0.022, 0] corresponding to classes BS, D, FB, PB, PS, and S, respectively. Hence, our final prediction for this test sample will be class PB with a probability of 0.825.

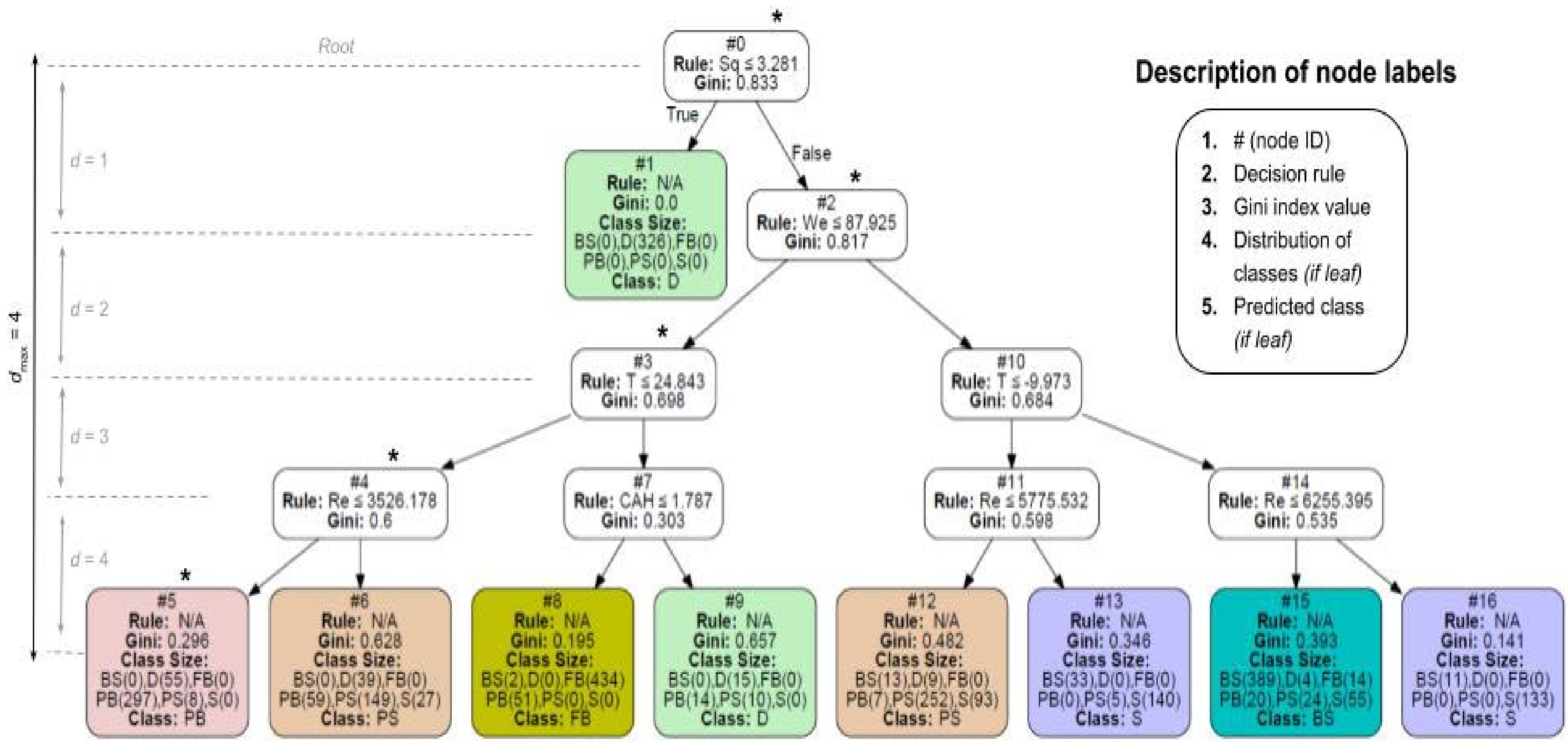

Fig.5 Tree structure and parameter values of our trained decision tree (DT) (d_{max} = 4). The asterisks (over selected nodes) indicate the decision path of the class inference of the exemplary test sample discussed in Section 2.4.1.1

2.4.1.2. Logistic Regression

The class probabilities in this model are described through softmax functions. From the trained parameters and the equation above (Eq. 2), the class probabilities can be described as:

$$P(y=D \mid x) \propto \exp(0.004-0.097\ T-0.003\ Re+0.064\ We+0.004\ CA+0.454\ CAH-0.021\ S_q), \quad \text{Eq.3}$$

$$P(y=PB \mid x) \propto \exp(0.317\ T-0.002\ Re-0.049\ We+0.044\ CA-0.23\ CAH+0.044\ S_q), \quad \text{Eq.4}$$

$$P(y=FB \mid x) \propto \exp(-0.002-0.079\ T+0.005\ Re-0.046\ We-0.103\ CA-0.09\ CAH-0.024\ S_q), \quad \text{Eq.5}$$

$$P(y=PS \mid x) \propto \exp(-0.023\ T-0.003\ Re+0.04\ We+0.089\ CA-0.066\ CAH), \quad \text{Eq.6}$$

$$P(y=BS \mid x) \propto \exp(-0.119\ T-0.001\ Re+0.032\ We+0.029\ CA+0.073\ CAH-0.022\ S_q), \text{ and} \quad \text{Eq.7}$$

$$P(y=S \mid x) \propto \exp(-0.001+0.002T+0.004Re-0.041\ We-0.064\ CA-0.141\ CAH+0.218\ S_q). \quad \text{Eq.8}$$

Note that these equations do not indicate equalities. The right-hand side of each equation is proportional to the corresponding class probability. The exact class probabilities can be obtained by normalizing these values by their summation. To predict the class label of a test sample, we can simply compute all the right-hand sides of the equations and then select the class having the highest score among all the classes.

These LR-based equations are a powerful means of modeling multilabel outcomes, such as the various phenomena (deposition, full bouncing, partial bouncing, and splashing, etc.) that occur during a droplet impact on a solid surface to measure the statistical significance of each independent variable with respect to probability. To better understand how to make class predictions with LR, let us consider a test sample with the feature x = [T, *Re*, *We*, CA, CAH, S_q] = [25, 4237.42, 85.9, 162.8, 1.3, 7.54]. Inserting these values into the class probability equations produces the non-normalized class scores: [91.65, 0.00, 11.44, 94.84, 0.00, 0.16], implying that the fourth class (i.e., PS) is assigned the largest score and is therefore the predicted class. The second and fifth classes (D and BS, respectively) obtained near-zero scores. Normalizing these values by division to their summation will give us a probability distribution that can be interpreted as the certainty of our trained LR model regarding the predicted class. For this test example, the probability distribution is [0.46, 0.00, 0.06, 0.48, 0.00, 0.00], implying that our model probabilistically infers that this sample belongs to Class 1 (S) with a probability of 46%, Class 3 (PB) with a probability of 48%, and Class 4 (PS) with a probability of only 6%.

3. Results and Discussion

3.1. Outcome of Droplet Impact Dynamics

We first investigated the influence of surface temperature on impact dynamics by varying the substrate temperature (−20, −10, and 25 °C) while maintaining the initial droplet temperature at room temperature. For the 25 °C experimental results, we relied on some previously published data from our lab [42]. As illustrated in Fig. 6, the water droplets vary in their impact behaviors on the surfaces, including full bouncing (FB), partial bouncing (PB), deposition (D), prompt splashing (PS), bouncing-splashing (BS), and splashing (S) [23].

FB PB D PS BS S

Fig. 6 Droplet impact regimes on silicone rubber surfaces. Regimes include full bouncing (FB, T = 25 °C, S_q = 7.54 µm, *We* = 15.81), partial bouncing (PB, T = −10 °C, S_q = 6.64 µm, *We* = 45.25), deposition (D, T = −10 °C, S_q = 1.76 µm, *We* = 16.81), prompt splashing (PS, T = −10 °C, S_q = 7.9 µm, *We* = 62.37), bouncing-splashing (BS, T = −10 °C, S_q = 7.9 µm, *We* = 142.62), and splashing (S, T = −10 °C, S_q = 7.54 µm, *We* = 208.74)

Impacting a droplet on hydrophilic, hydrophobic, and superhydrophobic surfaces alters the resulting regime in terms of deposition, bouncing, splashing, etc. Spreading or sticking of droplets can be observed when the test surfaces are hydrophilic or hydrophobic. In contrast, droplet mobility increases on superhydrophobic surfaces having a low CAH. The kinetic energy of the impacting droplet on the hydrophobic and superhydrophobic surfaces is converted into surface energy, and a small amount of energy is lost through viscous dissipation energy. Balances between inertia, viscosity, and capillary forces control the dynamic of droplets [20]. Surface properties, such as wettability, roughness, and temperature, markedly affect the bouncing and deposition of droplets; at lower temperatures, for example, the losses from viscous dissipation increase and lead to less available energy for bouncing. Therefore, the probability of bouncing decreases at lower temperatures [48].

Impacting water droplets at cold temperatures (−10 and −20 °C) operated in five regimes, i.e., deposition, partial bouncing, splashing, prompt splashing, and a transition regime between bouncing and splashing (Fig. 7). Fig. 7a1, a2 shows the dimensionless parameters for droplets hitting a hydrophobic surface (CA = 116°, CAH = 46.5°). For all *Re* and *We* numbers between 1380 and 7480 and 9 and 267, respectively, deposition occurs, and the liquid droplet cannot rebound. At lower *Re* and *We* numbers (*Re* <5293 and *We* <134 at –10 °C, *Re* <4646 and *We* <103 at –20 °C) for a non-water-repelling superhydrophobic surface of roughness 3.29 µm, the deposition of droplets and a prompt splashing occurs (Fig. 7b1,b2)), whereas at higher *Re* and *We* numbers, the impinging droplets splash.

Droplet impingement on water-repellent superhydrophobic surfaces having a lower CAH and varying roughness values (6.64, 7.54, and 7.9 µm) is shown in Fig. 7c–e, respectively. Depending on the surface roughness value, partial bouncing, deposition, splashing, prompt splashing, and bouncing-splashing can occur. At lower *Re* and *We* numbers, the droplets experience partial bouncing on these water-repellent surfaces. At intermediate *Re* and *We* numbers, prompt splashing occurs, and eventually, the droplets show a splashing behavior at higher *Re* and *We* numbers. Droplets were not deposited during the impact process for the superhydrophobic surface with the highest CA, highest roughness, and lowest CAH, although the probability of bouncing-splashing increases as surface roughness is greater for these surfaces at –10 °C.

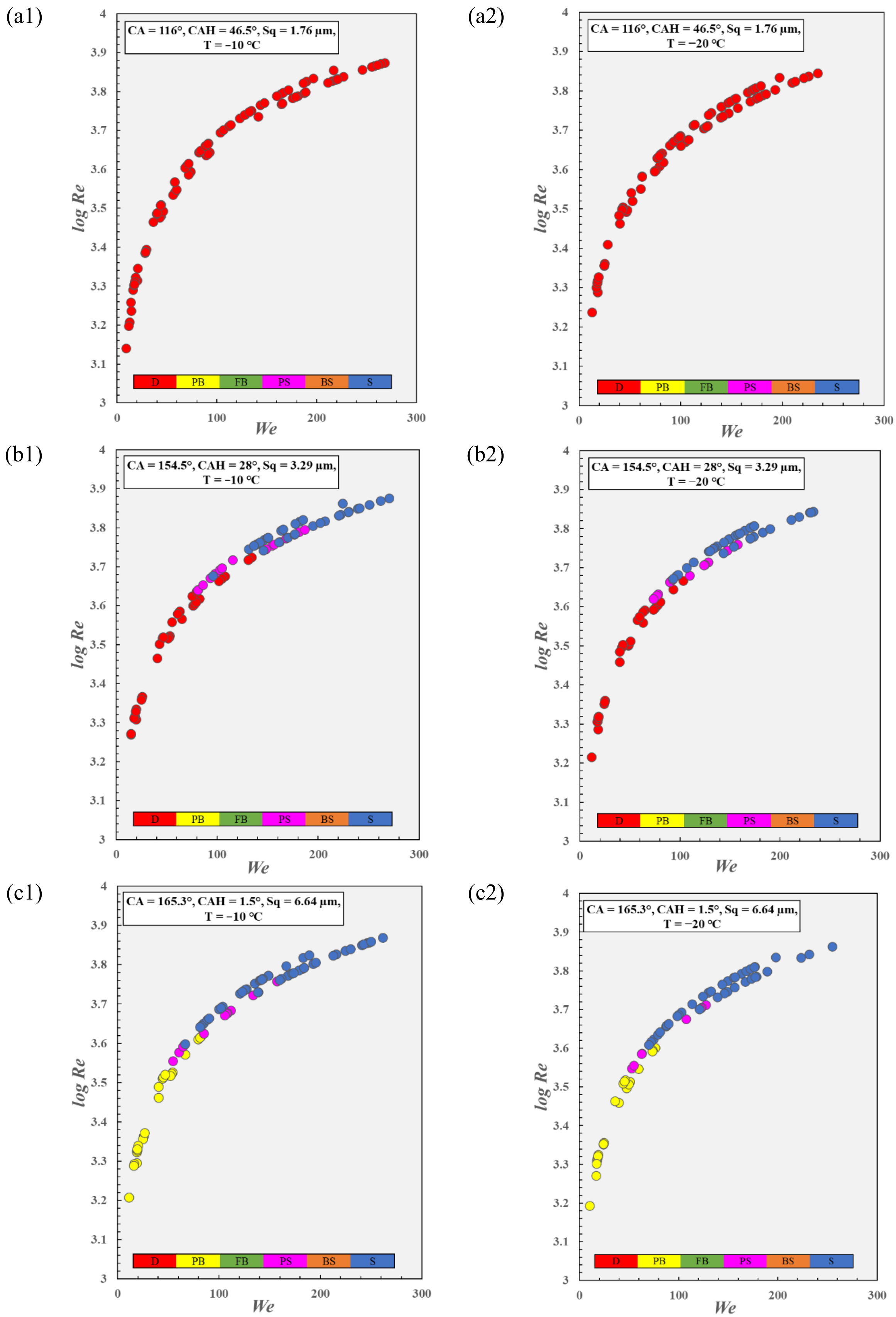
(a1)
CA = 116°, CAH = 46.5°, Sq = 1.76 µm,
T = −10 °C
(a2)
CA = 116°, CAH = 46.5°, Sq = 1.76 µm,
T = −20 °C
(b1)
CA = 154.5°, CAH = 28°, Sq = 3.29 µm,
T = −10 °C
(b2)
CA = 154.5°, CAH = 28°, Sq = 3.29 µm,
T = −20 °C
(c1)
CA = 165.3°, CAH = 1.5°, Sq = 6.64 µm,
T = −10 °C
(c2)
CA = 165.3°, CAH = 1.5°, Sq = 6.64 µm,
T = −20 °C
D
PB
FB
PS
BS
S
log Re
We
3
3.1
3.2
3.3
3.4
3.5
3.6
3.7
3.8
3.9
4
0
100
200
300

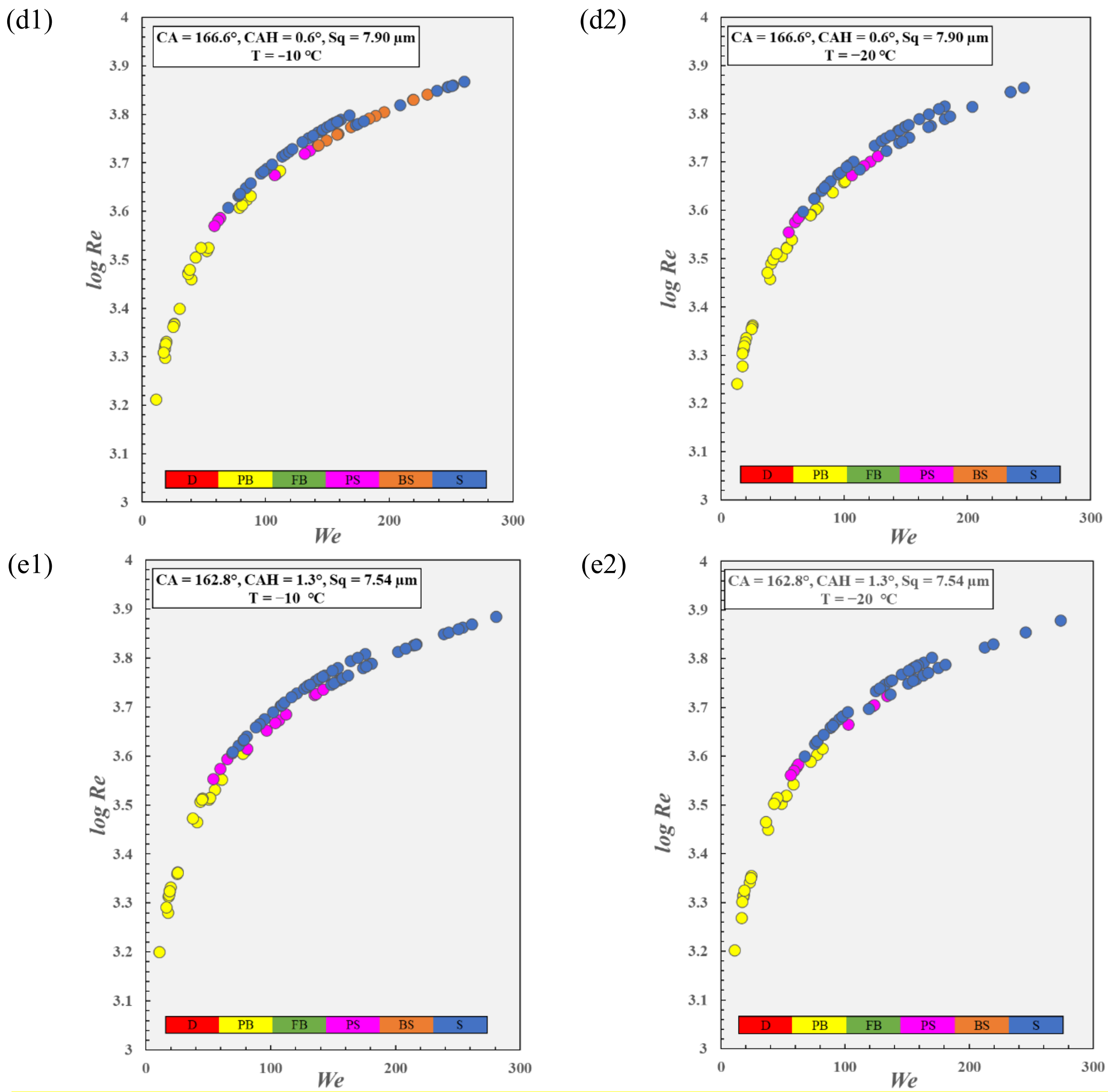

Fig. 7 Impact dynamics on silicone rubber surfaces: **a1** S_q = 1.76 μm, T = –10 °C; **a2** S_q = 1.76 μm, T = –20 °C; **b1** S_q = 3.29 μm, T = –10 °C; **b2** S_q = 3.29 μm, T = –20 °C; **c1** S_q = 6.64 μm, T = –10 °C; **c2** S_q = 6.64 μm, T = –20 °C; **d1** S_q = 7.90 μm, T = –10 °C; **d2** S_q = 7.90 μm, T = –20 °C; **e1** S_q = 7.54 μm, T = –10 °C; **e2** S_q = 7.54 μm, T = –20 °C

Fig. 8 a–e shows the impacting droplet behaviors at three surface temperatures for five different hydrophobic and superhydrophobic substrates. We observe that the effect of temperature is negligible for hydrophobic substrates and for non-water-repelling superhydrophobic surfaces having a roughness of 3.29 μm (Fig. 8 a, b). Impacting droplets are not affected by low temperatures on substrates 1 and 2. For the droplet impact on hydrophobic substrate 1, all operating conditions promote the spreading of the droplet;

however, for non-water-repelling superhydrophobic substrate 2, having a lower Weber number (<130), deposition occurs.

When observing impacting droplets on water-repellent superhydrophobic substrates (Fig. 8 c–e), we note that at low droplet velocity, the superhydrophobic surfaces of varying roughness (6.64, 7.54, and 7.9 μm) had better water repellency at sub-zero temperatures. These water-repellent superhydrophobic substrates reduce the probability of rebounding at lower temperatures. Droplets can partially or completely bounce off all water-repellent superhydrophobic surfaces at temperatures above 0 °C for We <110 and Re <5000; however, as the temperature of the surfaces is reduced, droplets show partial bouncing on the same substrates (having the same We values of <110), which related to the viscous dissipation.

Increasing the impact velocity of the droplet on rough surfaces heightens the probability of splashing (Fig. 8), as has been reported in other studies [49,50]. However, increased droplet velocity reduces the probability of bouncing, particularly at low temperatures; for example, we did not find conditions in which full bouncing could be observed at low temperatures. In contrast, at room temperature, we observe the complete retraction of water on water-repellent superhydrophobic surfaces (green symbol in Fig. 8). The most commonly observed behaviors of droplet dynamics on superhydrophobic surfaces at room temperature are complete bouncing, partial bouncing, and splashing [21].

Temperature, therefore, has a minor effect on droplet dynamics on cold hydrophobic and superhydrophobic silicone rubber surfaces for a wide range of We numbers and substrate temperatures. A possible reason for this temperature-independent nature of droplet impacting is the delay of solidification. A spreading velocity greater than that for solidification, even in the case of solidification at the early stages of drop impact, leads to this limited influence of sub-zero temperatures on droplet impact [34].

Another reason relates to heat transfer [48]. A rougher superhydrophobic surface characterized by a low CAH can entrap more air pockets in the interface between the surface and the water droplet. This entrapment reduces the contact area with the droplet and acts as an insulator to heighten the heat transfer barrier. The reduced contact area and heat transfer ability of superhydrophobic surfaces efficaciously limit increases in viscosity by decreasing the temperature. The reduced heat transfer from a cold hydrophobic or superhydrophobic surface to a droplet at high *We* numbers can limit water droplet dynamics on these surfaces. Therefore, substrate temperature has a similar but weaker effect on the superhydrophobic substrates at higher droplet velocities.

Moreover, the effect of surface temperature on droplet bouncing at lower *We* numbers for water-repellent superhydrophobic silicone rubber surfaces can be explained by the extent of energy dissipation and the wetting transition within the surface structures. Lower temperatures increase the viscosity of droplets, thereby increasing contact time and viscous dissipation while reducing the probability of bouncing. Moreover, surface wettability is significantly influenced by temperature. The wetting transition of a Cassie-Baxter to a Wenzel state by decreasing the temperature can reduce droplet bouncing [21,51].

Therefore, unlike many previous studies that examined the impact behavior of water droplets on cold superhydrophobic surfaces with a limited set of parameters, we investigated the effects of a wider range of influencing factors [31–34]. In general, for a wide range of *We* and *Re* numbers, our experimental results showed that the temperature has a minor impact on droplet dynamics on cold hydrophobic or superhydrophobic silicone rubber surfaces while previous studies reported a strong temperature dependency for the impact dynamics of water droplets [30,31,48]. Increasing *We* number and surface roughness, heightens the probability of splashing, as has been reported in other studies [49,50,52].

We then examine all possible variables simultaneously using machine-learning methods in the next section to analyze droplet regime; however, many of works do not include an analysis that incorporates multiple factors simultaneously [48,53,54]. Many studies have reported the use of machine learning techniques in material science, superhydrophobicity and icephobicity [40,41,54,55]. In this work we describe to the best of our knowledge the first application of machine learning to the detailed dynamic of water droplets impacting hydrophobic and superhydrophobic surfaces at different temperatures. Although the number of publications focused on droplet impact dynamics has increased recently, various aspects need study for the design of high-performance technical devices. The complexities of the impact process and the interaction of various influencing parameters could show the promise of the machine-learning approach. Therefore, if the dynamic behavior of droplets can be predicted before conducting experiments, assessing the performance of droplet-based devices and industrial applications can be done more accurately and effectively.

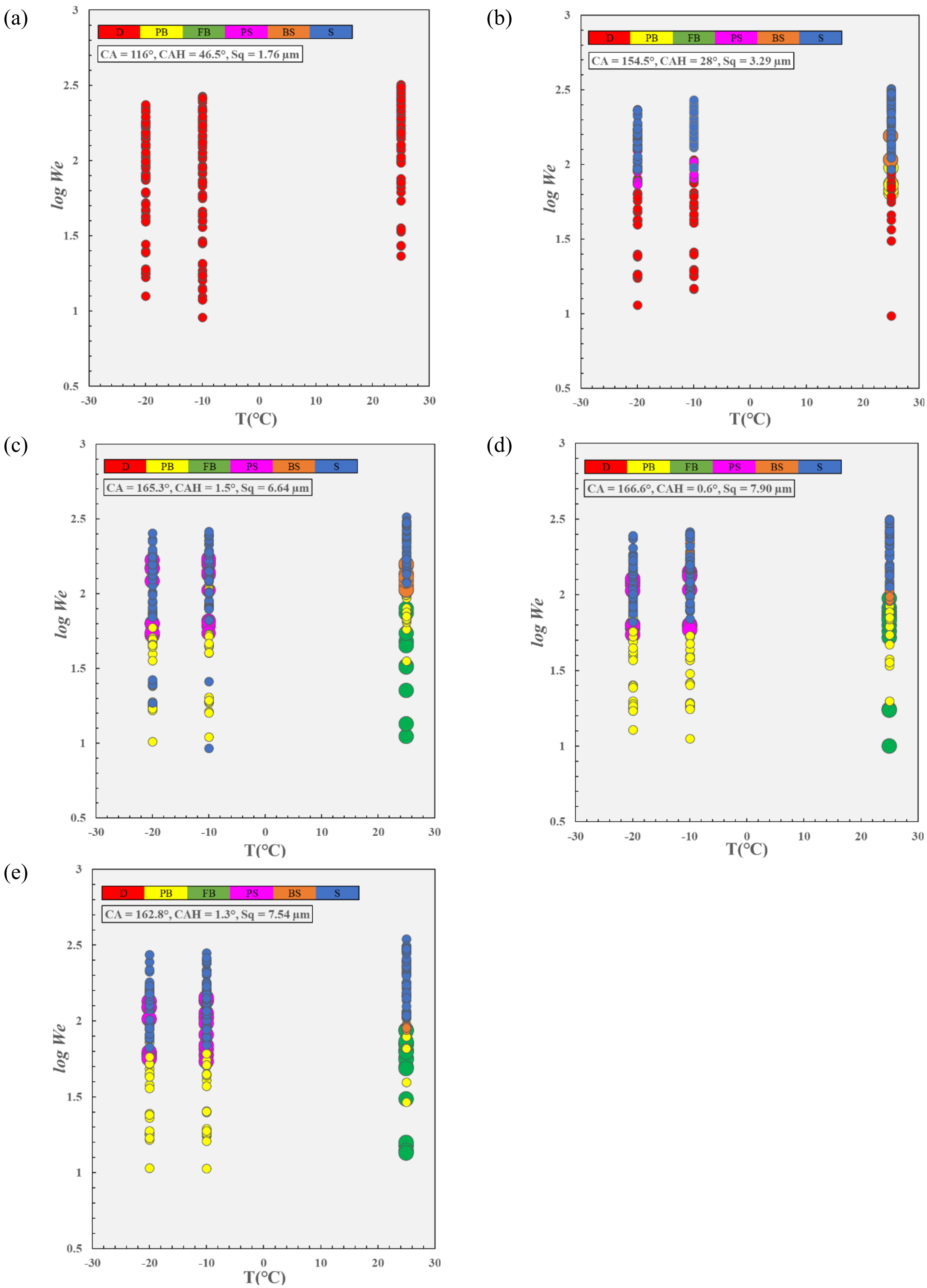
(a)
D PB FB PS BS S
CA = 116°, CAH = 46.5°, Sq = 1.76 µm
log We
T(°C)
(b)
D PB FB PS BS S
CA = 154.5°, CAH = 28°, Sq = 3.29 µm
log We
T(°C)
(c)
D PB FB PS BS S
CA = 165.3°, CAH = 1.5°, Sq = 6.64 µm
log We
T(°C)
(d)
D PB FB PS BS S
CA = 166.6°, CAH = 0.6°, Sq = 7.90 µm
log We
T(°C)
(e)
D PB FB PS BS S
CA = 162.8°, CAH = 1.3°, Sq = 7.54 µm
log We
T(°C)

Fig. 8 Droplet impact dynamics regime map for silicone rubber surfaces **a** S_q = 1.76; **b** S_q = 3.29; **c** S_q = 6.64; **d** S_q = 7.90; and **e** S_q = 7.54 µm at different temperatures

3.2. Classification Results

We trained and evaluated the three classifiers on a data set that we obtained from our experiments of impacting droplet behavior on silicone rubber surfaces (hydrophobic to superhydrophobic surfaces). Our data set consisted of six-dimensional feature vectors (T, *Re*, *We*, CA, CAH, and S_q) and six classes (FB, PB, D, PS, BS, and S). We randomly split the data into training and test partitions; the training set served for fitting the models, and the test data were kept for evaluating the model. The impact drop regimes show a highly imbalanced distribution (Fig. 9). To correct this imbalance between regimes, we augmented the training data using the *synthetic minority oversampling technique* (SMOTE) [56]. Oversampling ensures an equal number of training samples for each class; however, the test data were untouched and hence remained with an uneven distribution between classes. We had 2,688 training samples and 257 test samples following this preprocessing step.

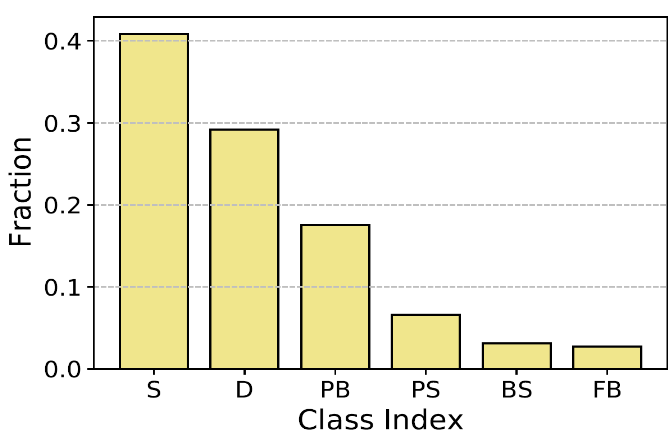

Fig. 9 Histogram of classes within the initial data set before the use of SMOTE. Splashing (S) is the dominant class (class 1), whereas bouncing-splashing (BS, class 2) and full bouncing (FB, class 3) are the least represented classes. Other classes are partial bouncing (PB, class 4), deposition (D, class 5), and prompt splashing (PS, class 6)

We used precision and recall to evaluate the performance of the trained classifiers. These criteria are specifically designed to be used with imbalanced data sets. In a binary positive/negative classification scenario, precision indicates the portion of the model's positive predictions that truly belong to the positive class. Recall measures how well the predictions cover the entire positive class. A low precision implies a high rate of false positives, whereas a low recall indicates many false negatives within the predictions. To summarize these two criteria, we used the F_1 score, defined as the harmonic mean of the two. This score is also originally proposed for binary classification problems and is defined as $F_1 = \frac{2\,Pr.Rc}{(Pr+Rc)}$, where $Pr = \frac{TP}{TP+FP}$ and $Rc = \frac{TP}{TP+FN}$ are precision and recall, respectively, and TP, FP, and FN denote the number of true positives (test samples with positive class in reality and in prediction), false positives (test samples with negative class in reality but positive in prediction), and false negatives (test samples with positive class in reality but negative in prediction), respectively. For multiclass problems like ours, F_1 is reported as the (weighted) average of F_1 scores individually evaluated for one-versus-rest of each class. In the case of weighted averaging, the score of each class is weighted according to its sample size, hence taking into account the existing class imbalance.

Table 2 summarizes the evaluation results of each classifier involved in our experiments. As is shown by our results, all the machine learning models were capable of predicting class labels though with different levels of accuracy; however, these results confirm the inferior classification ability of the linear LR model, showing that this model could not separate the training samples accurately and demonstrates the nonlinearity of the decision boundaries between the classes in our data sets. The model yielding the highest test accuracy had the highest complexity (non-linearity), which was expected as classifying real-world data usually demands highly non-linear models. Now as the complexity of learning models grows, interpretability of their outcomes become more challenging. More specifically, if one needs to translate the resulting prediction into a handful of simple algebraic rules, one would have to apply simpler (or even linear) techniques. Such interpretability power comes with a cost, i.e., a more modest generalization accuracy. Some relatively shallow DT (e.g., d_{max} = 7) are competitive against the deeper unconstrained DT (d_{max} = NA) or RF models in classifying the unseen test samples; however, they severely underperform when explaining the training data set. This observation indicates that the generalizability of classification models does not always linearly increase with their complexity.

Table 2 F_1 scores of the trained classifiers. Note that for the training data set, the weighted and unweighted average F_1 are the same because the class labels have been balanced through oversampling. Decision-tree (DT) models are trained using different d_{max} values and without any depth-dependent conditions (d_{max} = NA)

Metric (%)	DT (evaluated for various d_{max})								RF	LR
	4	5	6	7	8	9	10	NA		
Training										
F_1 (av.)	79.3	82.89	88.44	91.3	93.73	95.38	97.0	100	100	77.3
Test										
F_1 (av.)	63.15	63.41	67.91	74.18	71.08	69.66	71.88	73.54	75.19	60.21
F_1 (weighted av.)	74.6	72.99	80.99	86.05	85.47	85.3	86.11	87.44	89.04	77

In calculating the F_1 score, the predictions are obtained by selecting the class having the highest probabilities computed through the predictive model. For instance, computing F_1 in a binary classification is associated with placing a threshold for the positive class probabilities at 0.5. To obtain a more detailed portrait of the performance of a binary predictive model, we can change this threshold from 0 to 1 to obtain a range of F_1 scores or precision-recall pairs. Plotting the resulting precision versus the recalls yields what is usually called the precision-recall curve. An ideal classifier results in a recall and precision unit that is independent of the applied threshold; hence, the area under its precision-recall curve is 1. Fig. 10 presents the precision-recall curves of the LR and RF classifiers operating in a one-versus-rest mode for each class. DT is not considered here because trees that are not too shallow (e.g., d_{max} = NA) typically assign degenerative class probabilities to samples (therefore, zero uncertainty); there are thus very few operating points on the precision-recall curve. We then compared our classifiers with random baselines, for which the precision remains constant and equal to the size ratio of the corresponding class (equivalent to the positive-to-negative class ratio of the corresponding one-versus-rest binary classification).

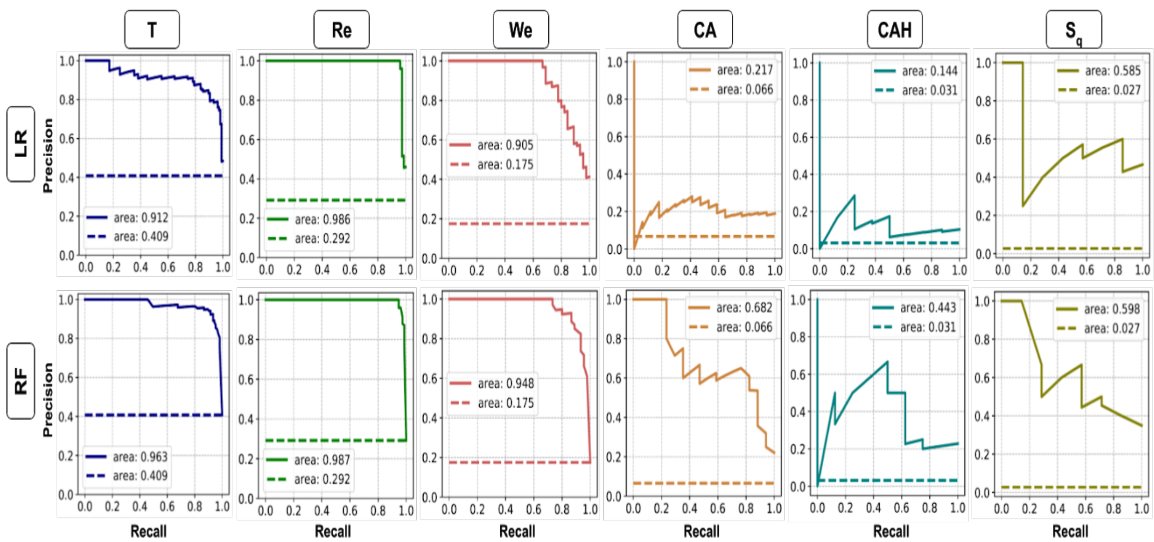

Fig. 10 Precision-recall curves of the logistic-regression (LR) and random-forest (RF) classifiers. Each graph indicates the curves for binary classification of an individual class versus the rest (one-versus-rest). The dashed lines represent random classifiers that have constant precision-recall curves for any classification problem

Fig.11 shows confusion matrices for the trained classifiers to better illustrate a binary comparison between the classes in the results. The (i,j)-th element of a confusion matrix shows the (normalized) count of samples that actually belong to class i but have been classified as class j. As can be observed in this figure, a common mistake among all the models is misclassifying samples of class BS as class S. In addition, a mistake that both our non-linear models (DT and RF) have committed is mistaking FB samples for class PB, whereas the linear model (LR) incorrectly labeled a significant number of PS samples as PB.

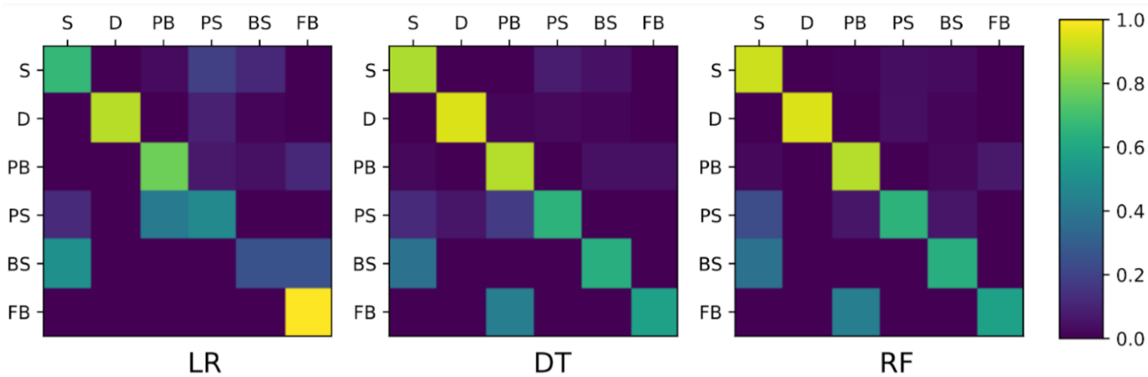

Fig. 11 Confusion matrix for the trained classifiers. The elements are normalized over the rows to compensate for the imbalancedness of the test data set.

A completely different working condition of these three algorithms would lead to different results and prediction accuracy. For example, a particular formula for classifying and predicting is used for LR, whereas RF works by constructing nodes and trees. The classification model of impact droplets on hydrophobic and superhydrophobic silicone rubber surfaces obtains satisfying results on the basis of the algorithms tested on the experimental data. Linear-based algorithms (LR) are not as accurate as the more sophisticated and nonlinear algorithms (DT and RF) for classifying impact droplets in scenarios of more complex experimental conditions. This leads to inaccuracies; however, LR is slightly more effective than DT and RF at producing understandable and interpretable equations. Consequently, the strong performance of our models indicates their ability to determine the complex relationship between the various parameters affecting impact droplets.

3.2.1. Analyzing the Importance of Features

The main objectives of the classification techniques are (1) predicting the output for new input features as accurately as possible and (2) providing information about the relationship between the input variables and output. Some of these models are linear classification models (e.g., LR) that are understandable and interpretable; however, these models may not perform better than nonlinear models.

One of the critical inputs to these machine-learning algorithms is the feature importance measurement, which can have various applications, such as reducing the number of dimensions and selecting the most contributing factors in a given data set [57,58]. Depicting a one-to-one relationship between impact behavior and the experimental parameters (including *Re*, *We*, CA, CAH, S_q, and T) is possible; however, in this conventional approach, quantifying variable importance is particularly challenging in the case of nonlinear relationships between parameters. Moreover, evaluating the simultaneous effect of each conditioning factor on impact behavior appears impossible through conventional methods.

We used multiclass supervised learning with a multitude of features to solve our classification task. We evaluate the performance of our models when all features are considered simultaneously. However, we can also isolate individual features and assess their respective importance in the classification. To perform the latter, we must apply distinct strategies for tree-based models (DT and RF) and logistic regression.

As explained above, decision trees comprise several nodes, each of which includes a decision rule as a function of a single feature. Here, we define the importance of each feature as the average reduction of the impurity criterion caused by that feature. Because we use the Ginni index to measure the impurity, the resulting score is also called the Ginni importance.

In the LR approach, we utilize the amount of change in the log-likelihood objective function of the LR model that is caused by a particular feature to measure its importance. More specifically, we repeat the training after removing a feature from the training data set and compute the log-likelihood objective function of the resulting model (excluding the regularization penalty term). The magnitude of the difference between the log-likelihood of the modified and original training models is the importance score of the considered feature.

In predicting the impact droplet process, the contribution of the different affecting parameters, their effectiveness, and their influence on the accuracy of the predictive models is critical. To demonstrate this, we present the relative importance of features (*Re*, *We*, CA, CAH, S_q, and T) for the three models (Fig. 12). Here, we consider the DT model without any depth-dependent conditions. We observe that all the models agree that T and *Re* are essential features to be retained. RF also assigns high importance to *We* number.

Interestingly, RF estimated that the *We* and *Re* numbers are the most important variables. T is the most important feature for surface properties, followed by CA, CAH, and S_q. Our experimental results (Figs. 7, 8) show that the *Re* and *We* numbers are the key factors affecting droplet behavior. For example, we observed a similar pattern for all water-repellent superhydrophobic silicone surfaces; however, depending on the selected *Re* and *We* numbers, it provoked either full bouncing, partial bouncing, deposition, splashing, prompt splashing, or bouncing-splashing. In this study, RF models perform better in analyzing feature importance given their agreement with the experimental results. Moreover, looking specifically at the dynamics of impacting droplets under icing conditions, as water droplet properties and wetting properties depend on temperature, it seems difficult to say that there is a linear relationship between these factors. This issue also highlights that using nonlinear algorithms such as RF to classify droplet behaviors under more complex experimental conditions is a valid and accurate approach for predicting droplet impact dynamics.

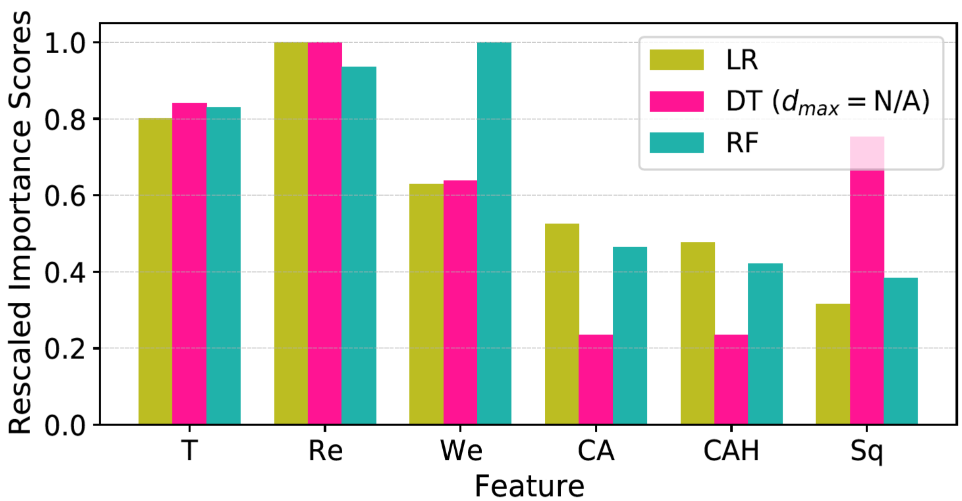

Fig. 12 Importance analysis of the features; temperature (T), Reynolds number (*Re*), Weber number (*We*), contact angle (CA), contact angle hysteresis (CAH) and surface roughness (S_q)) for the three trained models of logistic regression (LR), decision tree (DT), and random forest (RF)

4. Conclusion

Here we studied droplet impacts on hydrophobic and superhydrophobic surfaces at different temperatures and proposed design guidelines for nonwetting surfaces under droplet impingement. We applied experimental and statistical approaches to analyze the impact dynamics of water droplets at −20, −10, and 25 °C and discussed the influence of the substrate roughness, temperature, and wetting properties. The experiments showed that full bouncing observed only on superhydrophobic having a CA>160° and a CAH < 2°; and temperature has a minor effect on droplet dynamics on cold hydrophobic and superhydrophobic silicone rubber surfaces for a wide range of *We* numbers and different substrate temperatures. Multiple machine-learning methods were used to predict the temperature-dependent droplet behavior on hydrophobic and superhydrophobic silicone rubber surfaces, taking into consideration the impact velocity, droplet diameter, and surface features (CA, CAH, Sq, and T). Our logistic regression–based models produced equations for probability, and we combined experimental findings to model multilabel outcomes of different phenomena arising during droplet impact on a solid surface. We also used both linear (LR) and nonlinear (DT and RF) methods to assess the importance of surface characteristics and found that *We* and *Re* numbers were the most important factors followed by factors related to surface T, then CA, CAH, and S_q.

To the best of our knowledge, this work presents the first application of machine learning to experimental results obtained for the detailed dynamic motions of a water droplet impacting hydrophobic and superhydrophobic surfaces at different temperatures. Our results provide a means of predicting droplet impact behavior through the application of statistical LR modeling and the data-mining DT and RF modeling. All three machine-learning approaches agreed well with the experimental results for classifying droplet behaviors. Although all models exhibited a reasonable performance, the lower accuracy of the LR model indicated that the correlation was nonlinear. The dependency of water droplet properties and wetting properties on temperature makes finding a linear relationship between these parameters difficult. Thus, modeling water droplet behavior on the basis of these factors is not straightforward using conventional methods, illustrating the utility of the machine-learning approach.

CRediT authorship contribution statement

Samaneh Keshvarzi: Conceptualization, Investigation, Methodology, Validation, Writing – original draft, Writing - review & editing. **Jamshid Sourati**: Conceptualization, Methodology, Software, Validation, Investigation, Writing - original draft, Writing - review & editing. **Gelareh Momen**: Conceptualization, Project administration, Supervision, Resources, Funding acquisition, Writing - review & editing. **Reza Jafari**: Conceptualization, Project administration, Supervision, Resources, Funding acquisition, Writing - review & editing.

Declaration of Interests

The authors declare that they have no known competing financial interests or personal relationships that could have appeared to influence the work reported in this paper.

Acknowledgments

The authors would like to acknowledge the financial support from Natural Sciences and Engineering Research Council of Canada (NSERC). Also, we would like to thank the help of Mr. Vahid Asghari for machine-learning programming and Mr. Khosrow Maghsoudi for sample preparation during the experiments.

References

[1] Y. Cao, Z. Wu, Y. Su, Z. Xu, Aircraft flight characteristics in icing conditions, Prog. Aerosp. Sci. (2015). https://doi.org/10.1016/j.paerosci.2014.12.001.

[2] R. Jafari, G. Momen, M. Farzaneh, Durability enhancement of icephobic fluoropolymer film, J. Coatings Technol. Res. 13 (2016) 405–412. https://doi.org/10.1007/s11998-015-9759-z.

[3] Z. Zhang, X.Y. Liu, Control of ice nucleation: Freezing and antifreeze strategies, Chem. Soc. Rev. 47 (2018) 7116–7139. https://doi.org/10.1039/c8cs00626a.

[4] K. Maghsoudi, E. Vazirinasab, G. Momen, R. Jafari, Icephobicity and durability assessment of superhydrophobic surfaces: The role of surface roughness and the ice adhesion measurement technique, J. Mater. Process. Technol. 288 (2021) 116883. https://doi.org/10.1016/j.jmatprotec.2020.116883.

[5] M. Farzaneh, C. Volat, A. Leblond, Anti-icing and de-icing techniques for overhead lines, in: Atmos. Icing Power Networks, 2008. https://doi.org/10.1007/978-1-4020-8531-4_6.

[6] P. Irajizad, S. Nazifi, H. Ghasemi, Icephobic surfaces: Definition and figures of merit, Adv. Colloid Interface Sci. (2019). https://doi.org/10.1016/j.cis.2019.04.005.

[7] Y. Zhuo, S. Xiao, A. Amirfazli, J. He, Z. Zhang, Polysiloxane as icephobic materials – The past, present and the future, Chem. Eng. J. (2021). https://doi.org/10.1016/j.cej.2020.127088.

[8] A. Azimi Yancheshme, G. Momen, R. Jafari Aminabadi, Mechanisms of ice formation and propagation on superhydrophobic surfaces: A review, Adv. Colloid Interface Sci. 279 (2020) 102155. https://doi.org/10.1016/j.cis.2020.102155.

[9] T.M. Schutzius, S. Jung, T. Maitra, P. Eberle, C. Antonini, C. Stamatopoulos, D. Poulikakos, Physics of Icing and Rational Design of Surfaces with Extraordinary Icephobicity, Langmuir. 31 (2015) 4807–4821. https://doi.org/10.1021/la502586a.

[10] S. Heydarian, R. Jafari, G. Momen, Recent progress in the anti-icing performance of slippery liquid-infused surfaces, Prog. Org. Coatings. (2021). https://doi.org/10.1016/j.porgcoat.2020.106096.

[11] X. Wu, X. Zhao, J.W.C. Ho, Z. Chen, Design and durability study of environmental-friendly room-temperature processable icephobic coatings, Chem. Eng. J. (2019). https://doi.org/10.1016/j.cej.2018.07.204.

[12] T. Vasileiou, T.M. Schutzius, D. Poulikakos, Imparting Icephobicity with Substrate Flexibility, Langmuir. 33 (2017) 6708–6718. https://doi.org/10.1021/acs.langmuir.7b01412.

[13] M. Abolghasemibizaki, R. Mohammadi, Droplet impact on superhydrophobic surfaces fully decorated with cylindrical macrotextures, J. Colloid Interface Sci. 509 (2018) 422–431. https://doi.org/10.1016/j.jcis.2017.09.030.

[14] S. Farhadi, M. Farzaneh, S.A. Kulinich, Anti-icing performance of

superhydrophobic surfaces, Appl. Surf. Sci. (2011). https://doi.org/10.1016/j.apsusc.2011.02.057.

[15] T. Vasileiou, T.M. Schutzius, D. Poulikakos, Imparting Icephobicity with Substrate Flexibility, Langmuir. (2017). https://doi.org/10.1021/acs.langmuir.7b01412.

[16] Z. Jin, Z. Wang, D. Sui, Z. Yang, The impact and freezing processes of a water droplet on different inclined cold surfaces, Int. J. Heat Mass Transf. (2016). https://doi.org/10.1016/j.ijheatmasstransfer.2016.02.024.

[17] G. Yang, K. Guo, N. Li, Freezing mechanism of supercooled water droplet impinging on metal surfaces, in: Int. J. Refrig., 2011. https://doi.org/10.1016/j.ijrefrig.2011.07.001.

[18] H. Li, I. V. Roisman, C. Tropea, J. Li, S. Fu, Water Drop Impact on Cold Surfaces with Solidification, in: AIP Conf. Proc., 2011: pp. 451–453. https://doi.org/10.1063/1.3651944.

[19] Z. Jin, D. Sui, Z. Yang, The impact, freezing, and melting processes of a water droplet on an inclined cold surface, Int. J. Heat Mass Transf. (2015). https://doi.org/10.1016/j.ijheatmasstransfer.2015.06.086.

[20] C. Josserand, S.T. Thoroddsen, Drop Impact on a Solid Surface, Annu. Rev. Fluid Mech. 48 (2016) 365–391. https://doi.org/10.1146/annurev-fluid-122414-034401.

[21] D. Khojasteh, M. Kazerooni, S. Salarian, R. Kamali, Droplet impact on superhydrophobic surfaces: A review of recent developments, J. Ind. Eng. Chem. 42 (2016) 1–14. https://doi.org/10.1016/j.jiec.2016.07.027.

[22] Z. Li, Q. Kong, X. Ma, D. Zang, X. Guan, X. Ren, Dynamic effects and adhesion of water droplet impact on hydrophobic surfaces: Bouncing or sticking, Nanoscale. (2017). https://doi.org/10.1039/c7nr02906c.

[23] A.L. Yarin, DROP IMPACT DYNAMICS: Splashing, Spreading, Receding, Bouncing…, Annu. Rev. Fluid Mech. 38 (2006) 159–192. https://doi.org/10.1146/annurev.fluid.38.050304.092144.

[24] X. Jiang, E. Xu, G. Wu, H.Z. Li, Drop impact on superhydrophobic surface with protrusions, Chem. Eng. Sci. 212 (2020) 115351. https://doi.org/10.1016/j.ces.2019.115351.

[25] M. Abolghasemibizaki, R. Mohammadi, Droplet impact on superhydrophobic surfaces fully decorated with cylindrical macrotextures, J. Colloid Interface Sci. (2018). https://doi.org/10.1016/j.jcis.2017.09.030.

[26] B.J. Murray, D. O'sullivan, J.D. Atkinson, M.E. Webb, Ice nucleation by particles immersed in supercooled cloud droplets, Chem. Soc. Rev. (2012). https://doi.org/10.1039/c2cs35200a.

[27] S. Kim, T. Wang, L. Zhang, Y. Jiang, Droplet impacting dynamics on wettable, rough and slippery oil-infuse surfaces, J. Mech. Sci. Technol. (2020). https://doi.org/10.1007/s12206-019-1223-z.

[28] Z. Jin, H. Zhang, Z. Yang, The impact and freezing processes of a water droplet on a cold surface with different inclined angles, Int. J. Heat Mass Transf. (2016). https://doi.org/10.1016/j.ijheatmasstransfer.2016.08.012.

[29] T. Maitra, M.K. Tiwari, C. Antonini, P. Schoch, S. Jung, P. Eberle, D. Poulikakos, Erratum: Nanoengineering of superhydrophobic and impalement resistant surface textures below the freezing temperature (Nano Letters (2014) 14:1 (172-182) DOI: 10.1021/nl4037092), Nano Lett. 14 (2014) 1106. https://doi.org/10.1021/nl500297b.

[30] Z. Jin, H. Zhang, Z. Yang, Experimental investigation of the impact and freezing processes of a water droplet on an ice surface, Int. J. Heat Mass Transf. (2017). https://doi.org/10.1016/j.ijheatmasstransfer.2017.02.055.

[31] L. Mishchenko, B. Hatton, V. Bahadur, J.A. Taylor, T. Krupenkin, J. Aizenberg, Design of ice-free nanostructured surfaces based on repulsion of impacting water droplets, ACS Nano. (2010). https://doi.org/10.1021/nn102557p.

[32] B. Ding, H. Wang, X. Zhu, R. Chen, Q. Liao, Water droplet impact on superhydrophobic surfaces with various inclinations and supercooling degrees, Int. J. Heat Mass Transf. 138 (2019) 844–851. https://doi.org/10.1016/j.ijheatmasstransfer.2019.04.106.

[33] L. Zheng, Z. Li, S. Bourdo, K.R. Khedir, M.P. Asar, C.C. Ryerson, A.S. Biris, Exceptional superhydrophobicity and low velocity impact icephobicity of acetone-functionalized carbon nanotube films, Langmuir. 27 (2011) 9936–9943. https://doi.org/10.1021/la201548k.

[34] H. Li, I. V. Roisman, C. Tropea, Influence of solidification on the impact of supercooled water drops onto cold surfaces, Exp. Fluids. 56 (2015) 1–13. https://doi.org/10.1007/s00348-015-1999-2.

[35] Y. Reich, S.V. Barai, Evaluating machine learning models for engineering problems, Artif. Intell. Eng. 13 (1999) 257–272. https://doi.org/10.1016/S0954-1810(98)00021-1.

[36] V. Asghari, Y.F. Leung, S.-C. Hsu, Deep neural network based framework for complex correlations in engineering metrics, Adv. Eng. Informatics. 44 (2020) 101058. https://doi.org/10.1016/j.aei.2020.101058.

[37] C. Li, D. Rubín De Celis Leal, S. Rana, S. Gupta, A. Sutti, S. Greenhill, T. Slezak, M. Height, S. Venkatesh, Rapid Bayesian optimisation for synthesis of short polymer fiber materials, Sci. Rep. 7 (2017) 1–10. https://doi.org/10.1038/s41598-017-05723-0.

[38] S. Ringdahl, S. Xiao, J. He, Z. Zhang, Machine Learning Based Prediction of Nanoscale Ice Adhesion on Rough Surfaces, Coatings. 11 (2020) 33. https://doi.org/10.3390/coatings11010033.

[39] A. Kordijazi, H.M. Roshan, A. Dhingra, M. Povolo, P.K. Rohatgi, M. Nosonovsky, Machine-learning methods to predict the wetting properties of iron-based composites, Surf. Innov. (2020). https://doi.org/10.1680/jsuin.20.00024.

[40] X. Zhang, B. Ding, R. Cheng, S.C. Dixon, Y. Lu, Computational Intelligence-Assisted Understanding of Nature-Inspired Superhydrophobic Behavior, Adv. Sci. 5 (2018). https://doi.org/10.1002/advs.201700520.

[41] S. Li, J. Qin, M. He, R. Paoli, Fast Evaluation of Aircraft Icing Severity Using Machine Learning Based on XGBoost, Aerospace. 7 (2020) 36. https://doi.org/10.3390/aerospace7040036.

[42] A. Azimi Yancheshme, S. Hassantabar, K. Maghsoudi, S. Keshavarzi, R. Jafari, G. Momen, Integration of experimental analysis and machine learning to predict drop behavior on superhydrophobic surfaces, Chem. Eng. J. 417 (2021) 127898. https://doi.org/10.1016/j.cej.2020.127898.

[43] G.G. Moisen, Classification and Regression Trees, 2008. https://doi.org/10.1016/B978-008045405-4.00149-X.

[44] A. Criminisi, J. Shotton, E. Konukoglu, Decision Forests for Classification , Regression , Density Estimation , Manifold Learning and Semi-Supervised Learning, 2011.

[45] R.M. Neal, Pattern Recognition and Machine Learning, Springer US, 2007. https://doi.org/10.1198/tech.2007.s518.

[46] R. Tibshirani, Regression Shrinkage and Selection Via the Lasso, J. R. Stat. Soc. Ser. B. (1996). https://doi.org/10.1111/j.2517-6161.1996.tb02080.x.

[47] A.E. Hoerl, R.W. Kennard, Ridge Regression: Biased Estimation for Nonorthogonal Problems, Technometrics. (1970). https://doi.org/10.1080/00401706.1970.10488634.

[48] A. Alizadeh, V. Bahadur, S. Zhong, W. Shang, R. Li, J. Ruud, M. Yamada, L. Ge, A. Dhinojwala, M. Sohal, Temperature dependent droplet impact dynamics on flat and textured surfaces, Appl. Phys. Lett. (2012). https://doi.org/10.1063/1.3692598.

[49] A. Latka, A. Strandburg-Peshkin, M.M. Driscoll, C.S. Stevens, S.R. Nagel, Creation of prompt and thin-sheet splashing by varying surface roughness or increasing air pressure, Phys. Rev. Lett. 109 (2012) 3–6. https://doi.org/10.1103/PhysRevLett.109.054501.

[50] R. Rioboo, C. Tropea, M. Marengo, Outcomes from a drop impact on solid surfaces,

At. Sprays. (2001). https://doi.org/10.1615/atomizspr.v11.i2.40.

[51] D. Bartolo, F. Bouamrirene, É. Verneuil, A. Buguin, P. Silberzan, S. Moulinet, Bouncing or sticky droplets: Impalement transitions on superhydrophobic micropatterned surfaces, Europhys. Lett. 74 (2006) 299–305. https://doi.org/10.1209/epl/i2005-10522-3.

[52] C. Tang, M. Qin, X. Weng, X. Zhang, P. Zhang, J. Li, Z. Huang, Dynamics of droplet impact on solid surface with different roughness, Int. J. Multiph. Flow. (2017). https://doi.org/10.1016/j.ijmultiphaseflow.2017.07.002.

[53] R. Zhang, P. Hao, X. Zhang, F. He, Supercooled water droplet impact on superhydrophobic surfaces with various roughness and temperature, Int. J. Heat Mass Transf. (2018). https://doi.org/10.1016/j.ijheatmasstransfer.2018.01.076.

[54] X. Wang, Z. Tang, B. Xu, Z. Chen, Anti-freezing characteristics of water droplet impinging the superhydrophobic surface: An experimental and predictive study, Appl. Surf. Sci. (2021). https://doi.org/10.1016/j.apsusc.2021.150717.

[55] Z. Yuan, S. Gao, Z.F. Hu, L. Dai, H. Hou, F. Chu, X. Wu, Ultimate jumping of coalesced droplets on superhydrophobic surfaces, J. Colloid Interface Sci. (2021). https://doi.org/10.1016/j.jcis.2020.12.007.

[56] N. V. Chawla, K.W. Bowyer, L.O. Hall, W.P. Kegelmeyer, SMOTE: Synthetic minority over-sampling technique, J. Artif. Intell. Res. (2002). https://doi.org/10.1613/jair.953.

[57] R. Wang, V. Asghari, S.C. Hsu, C.J. Lee, J.H. Chen, Detecting corporate misconduct through random forest in China's construction industry, J. Clean. Prod. (2020). https://doi.org/10.1016/j.jclepro.2020.122266.

[58] M. Saarela, S. Jauhiainen, Comparison of feature importance measures as explanations for classification models, SN Appl. Sci. (2021). https://doi.org/10.1007/s42452-021-04148-9.